A comprehensive study on the aerodynamic influence of stationary and moving obstacles on an isolated phantom DJI 3 UAV propeller

Charbel Hage, Tonino Sophy, El Hassane Aglzim

Received: 22 November 2023 | Revised: 9 March 2024 | Accepted: 14 March 2024

The Journal of Engineering

DOI: 10.1049/tje2.12374

The Institution of Engineering and Technology WILEY

ORIGINAL RESEARCH

A comprehensive study on the aerodynamic influence of stationary and moving obstacles on an isolated phantom DJI 3 UAV propeller

Charbel Hage | **Tonino Sophy** | **El Hassane Aglzim**

Univ. Bourgogne Franche-Comté, DRIVE Laboratory, Nevers, France

Correspondence
Charbel Hage, Univ. Bourgogne Franche-Comté, DRIVE Laboratory, F58000, Nevers, France.
Email: charbel.hage@u-bourgogne.fr

Funding information
Bourgogne Franche-Comte region, France (Région BFC)

Abstract

Unmanned aerial vehicle (UAV) technology is experiencing strong growth in many fields such as military and civil. When operating around obstacles and in the proximity of walls or moving objects, the UAV is constrained to thrust and power consumption variation induced by several aerodynamic effects that can lead to severe flight instability. In this paper, a methodology based on multiple reference frames (MRF) is developed and applied to computational fluid dynamics (CFD) simulations on a Phantom DJI 3 propeller to reproduce the effect of fixed and moving wall proximity on the propeller aerodynamic performances. When hovering (3000 rpm) at 0.2 m above a moving obstacle (15 m/s), the results have shown a huge decrease in the thrust by 11.3% when compared to fixed obstacle thrust. This effect, however, is reduced when the propeller is hovering at 5000 rpm and neglected at 9550 rpm. Finally, the moving obstacle had a significant impact on the propeller's aerodynamic performance, resulting in a decrease in thrust force and power consumption at low hovering rotational velocities. Especially, when the obstacle is moving at a fast speed, the UAV could properly use high rotational velocity to maintain high power loading and ensure hovering stability.

1 | INTRODUCTION

With the huge development of UAV technology in logistics and transportation applications such as cargo delivery, surface inspections, and more military and civil applications [1–3], numerous research endeavors are currently underway to enhance the safety of Unmanned Aerial Vehicle (UAV) flights within urban environments, particularly under specific circumstances. A primary challenge faced during the operation of small UAVs is their vulnerability to adverse weather conditions, strong winds, and air turbulence. This susceptibility stems from their diminutive size, slow cruising speeds, and limited endurance, as observed in the study by Graham and Murray in 2016 [4]. Furthermore, the interaction between external airflow and disturbances arising from the collision of the quadcopter propeller's downwash flow with both stationary and moving vehicles significantly influences the stability and aerodynamic performance of UAVs. Hence, it is imperative to investigate the aerodynamic properties of quadcopter propellers when they encounter fixed or mobile obstacles. Additionally, the introduction of obstacles such as walls, cars, buses, or trains further complicates the flow dynamics. The horizontal movement generated by these obstacles creates incoming airflow that interferes with the aerodynamic characteristics of the quadcopter propeller's downwash. Consequently, this results in a more intricate flow field, ultimately impacting the reliability and stability of quadcopter UAVs.

Currently, the latest theoretical and experimental investigations regarding the impact of ground effects on the thrust generated by a single propeller have not given due attention to the influence of moving obstacles and walls. Previous experimental inquiries have primarily centered around the examination of rotor rotation, rotor positioning, blade geometry, and the presence of a stationary ground on thrust, as documented in studies by Robert Kleike in 2017 and David Giurato in 2018 [5, 6]. Validation of the results, particularly for a single quadcopter propeller, has demonstrated strong agreement with the theoretical models established by Cheeseman and Bennett in 1955 [7]. Notably, the ground effect becomes noticeable at approximately $H/R < 2$, where H represents

ground height, and R represents propeller radius, in the case of a solitary propeller. For a quadcopter configuration, this effect becomes pronounced at $H/R < 4$, as described by Cheeseman and Bennett in their 1955 work. Furthermore, more intricate theoretical models, which build upon the Cheeseman and Bennett model, have been developed and subsequently compared with experimental outcomes to predict the fixed-ground effect on quadcopter performance. These models have been explored in studies conducted by Bangura in 2012, Li and Lu in 2015, Sanchez in 2017, Gao and Nicola in 2019, Xiang and Leang in 2020, and Mckinnon and Angela in 2020 [8–13].

Using Computational Fluid Dynamics CFD simulations, the common three ways that allow the modeling and the prediction of the actual 3D flow generated by a particular blade spinning at a specific angular speed are the use of Multiple Reference Frames (MRF), sliding meshes, and the dynamic meshes. Several numerical simulations were performed using the MRF method to reproduce the flow generated by the spinning propeller due to its low computational cost since the solution is steady and no transient simulations are required [14]. Contrary to the MRF model, the sliding mesh model requires transient simulations since the mesh is updated at each time step, which increases significantly the computational cost. Besides, the sliding mesh technique allows the mesh region around the blade to rotate, simulating the actual flow generated by the spinning blade. Sliding mesh models were employed in the studies of [15, 16] when studying the performance of the blades on wind turbines. The sliding mesh model considers a moving region, an external static region, and a sliding interface between the two regions. The mesh region that contains the propeller blade rotates at a specific speed and consequently, the blade wall is rotating at the same speed. Hence, the velocity vector of the fluid cells is modified and therefore reproduces realistically the downwash flow.

Close to the ground and when compared to each other, the MRF model underestimates the thrust but follows the curvature of the sliding mesh model and the theoretical ones proposed by [7]. The results and the performance of both methods were studied in detail by [17] and the results showed that the MRF method can accurately predict the thrust and the ground effect on one propeller with a significant decrease in temporal computational costs compared to the sliding Mesh model. To illustrate, in a simulation involving approximately 26 million elements, the MRF model achieved convergence in merely around 1000 h per processor. In contrast, the sliding Mesh model demanded a prolonged computational time ranging between 8000 and 9000 h per processor before a periodic transient cycle could be identified [17]. Besides, examining the magnitude of the MRF thrust normalized by the thrust obtained using the sliding model without the effect of the ground, the results showed also excellent agreement when compared together [17]. Moreover, despite showing favorable agreement, there is a significant difference of 9 to 12% in the results between the MRF model and the sliding model [17]. Considering this deviation, the notably reduced computational cost of the MRF model renders it a highly attractive option. Moreover, [18, 19] used MRF to simulate the flow of a single rotor, obtaining good agreement with experimental results. The examination of aerodynamic impacts on a quadcopter UAV's flight stability in close proximity to walls and the ground was conducted using the MRF model by Paz et al. [20]. This investigation aimed to study the aerodynamic effects of an obstacle as a quadcopter flies above it at a high rotational speed of 9550 rpm and a considerable moving velocity of 10 m/s. To ensure precision and reliability in the analysis, both steady and transient solvers were employed independently. The MRF model, specifically used for propellers, played a key role in both solvers. The transient solver was applied to simulate the drone's horizontal movement above the obstacle, incorporating a dynamic mesh to adapt to the changing geometry. Rigorous validation of the obtained results confirmed their accuracy and reliability.

In terms of research methodologies, assessing the aerodynamic performance of quadcopter UAVs when operating near obstacles presents a primary and intricate challenge due to the multitude of variables involved in such scenarios. For instance, researchers have resorted to employing a combination of wind tunnel tests along with other methodologies to study factors like the airflow generated by propellers, the ground effect arising from induced velocity, and the thrust produced by the UAV. These investigations have been documented in studies by [21–23]. Moreover, computational fluid dynamics (CFD) techniques have been employed for both 2D and 3D numerical analyses. Several approaches have been applied to forecast the downwash flow generated by quadcopters, as observed in studies conducted by [24–26]. However, none of these methods adequately replicates the intricate 3D flow generated by the propellers in the presence of moving obstacles at varying altitudes and velocities as experienced by the UAV.

In this line, the primary aim of the current paper is to replicate and assess the interaction between a Phantom DJI 3 drone's propeller and both stationary and moving obstacles while in a hovering flight configuration. This analysis utilizes the commercially available computational fluid dynamics (CFD) solver, FLUENT. Specifically, we investigate how the presence of a moving obstacle such as a car, bus, or train in close proximity to the propeller influences the flow of air around these vehicles and its subsequent impact on the propeller's thrust force and power parameters. It is important to note that a simplified planar surface wall approximation is treated in this research and overlooks the actual flow dynamics caused by the tramway roof which is more complex than a planar surface [27]. This scenario is frequently encountered, particularly within the context of the Deliv'Air project, which receives funding from the Bourgogne Franche-Comté region (Région BFC). The Deliv'Air project aims to operate delivery drones that can seamlessly utilize existing public transportation for swift and autonomous delivery flights. Throughout the phases of approach, landing, and takeoff, the UAV may encounter regions characterized by intense turbulence and fluid separation zones, potentially leading to control instability or necessitating adjustments in rotor settings for energy management.

Accordingly, we exclusively simulated the behavior of an isolated propeller within an environment featuring moving walls. The primary goal was to gain a deeper understanding of the

complex interactions between the propeller's downwash and the delicate airflow patterns generated by these moving walls. This investigation served a dual purpose: firstly, to explain the isolated propeller's unique aerodynamic behavior, devoid of the influence of neighboring propellers, and second, to predict its behavior when it operates in the proximity of moving obstacles, particularly in the context of larger quadcopters where each propeller can be considered in isolation due to their significant spatial separation.

Furthermore, the outcomes of our specific study hold significant practical implications for the field of UAV control and performance optimization. The detailed insights gained from simulating the behavior of an isolated propeller in the presence of moving walls can be instrumental in fine-tuning control algorithms. By leveraging these findings, we can enhance the UAV's stability during flights in proximity to moving obstacles. This optimization not only contributes to a smoother and more controlled flight experience but also carries the potential to extend the lifespan of the drone's battery. The improved efficiency in energy management, informed by a deep understanding of aerodynamic interactions, may lead to an overall increase in the drone's flight duration [27]. Such advancements align seamlessly with the goals of projects like Deliv'Air, where reliable and stable drone flights are crucial for successful and autonomous delivery operations.

Throughout the analyses of our study, an unstructured tetrahedral meshing is used with a k-ω Shear Stress Transport (SST) turbulence model. The Multiple Reference Frame model is used to consider the rotation of the propeller at several rotational speeds.

Hence, this contribution comprises four distinct sections. Following this introductory section, which can be found in Section 1, the subsequent Section 2 delves into the geometric model of the Phantom DJI 3 propeller, the fluid field partitioning, computational methods, and the boundary conditions for each simulation. Moving forward, Section 3 provides a comprehensive account of mesh validation and the rotation approach through a comparison with experimental data. Subsequently, Section 4 presents and discusses the primary findings of the study, encompassing velocity fields and aerodynamic parameters. Finally, Section 5 summarizes the research's key conclusions.

2 | MATERIALS AND METHODS

2.1 | Geometrical model

In this study, we utilized the propeller from the Phantom DJI 3 Standard quadcopter, a popular choice due to its widespread availability in the quadcopter market. The Phantom DJI 3 Standard quadcopter is equipped with four rotors, each having a diameter of 240 mm. Additionally, it includes a camera, its mounting assembly, and two support legs as part of its configuration (Figure 1).

Figures 2 and 3 provide descriptions of the 3D model of the propeller from the front, side, and its shape characteristics.

FIGURE 1 Phantom DJI 3 original geometry.

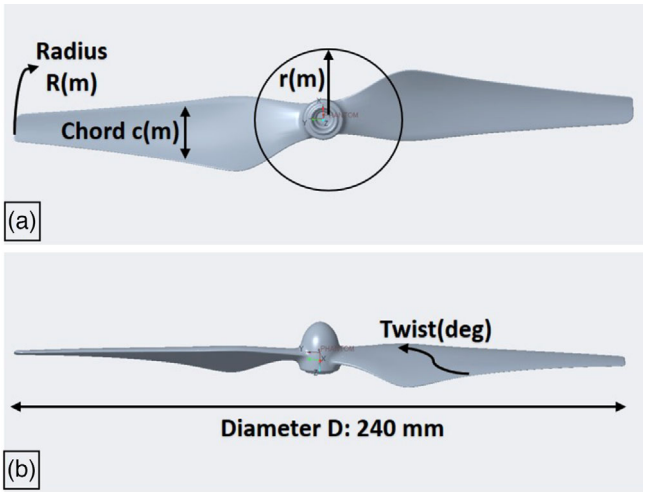

FIGURE 2 Phantom DJI 3 propeller: (a) Front view; (b) side view.

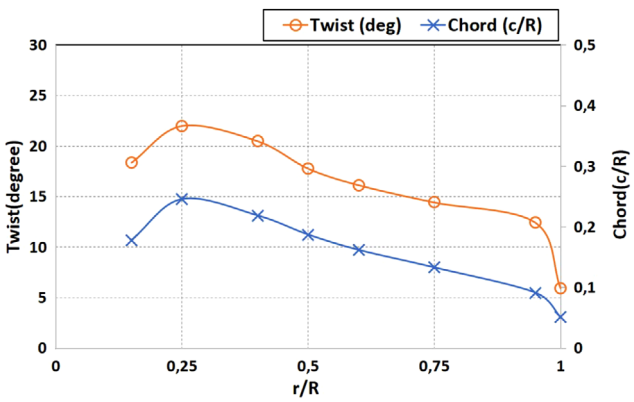

FIGURE 3 Phantom DJI 3 propeller characteristics.

The figure depicted in Figure 3 illustrates the chord width and the blade's twist angle across the radius, aligning with the original geometry's profile. The data presented in Figure 3 is derived from an experimental study conducted by Deters and Kleinke [5]. The chord and twist distribution for the propeller were measured using the PropellerScanner software created by Hepperle [28], as mentioned in their study [5]. It is also important to acknowledge the limitations highlighted by Uhlig et al. [29] regarding the PropellerScanner software, particularly

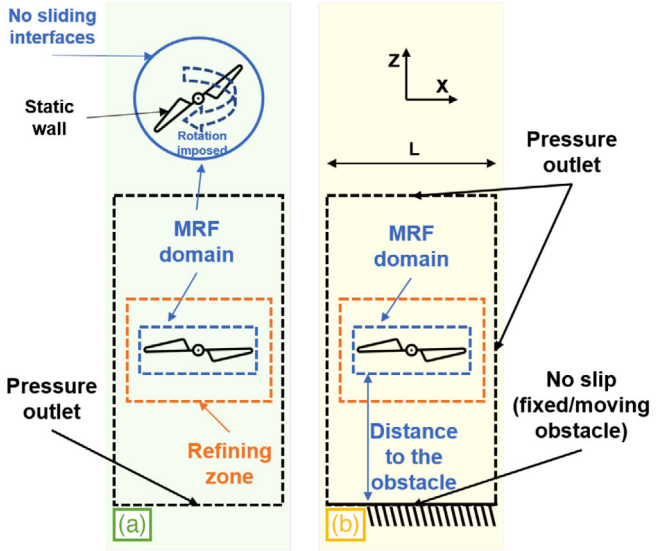

FIGURE 4 Scheme of different simulation settings used in this study: (a) preliminary propeller study, (b) main contribution study.

in underestimating twist angles compared to physical measurements. Despite this limitation, the software was chosen in their study for its capability to provide a convenient means of comparing propeller geometries.

2.2 | Numerical methodology and boundary conditions

Within this investigation, we employed two distinct simulation configurations to independently assess each of the components influencing the interaction between an open propeller and either a stationary or mobile wall. These two configurations, labeled as (a) and (b), are outlined in Figure 4 and elaborated upon in the following section.

The case depicted in Figure 4a has been employed for two primary purposes in this study. First, it serves as the basis for characterizing the airflow generated by the rotation of the propeller, a critical aspect when simulating the flight of a quadcopter. Additionally, it is used as a means of comparing the resulting forces with referenced experimental data, as documented in the study by [5]. Furthermore, a meticulous examination of mesh convergence was conducted at various propeller speeds to determine the optimal meshing parameters. In terms of the rotational technique employed, the Multiple Reference Frame (MRF) method was chosen and applied to replicate the propeller's rotation, as described in the work by [30]. This method was specifically applied to the fluid region directly adjacent to the propeller, enclosed within the blue cylindrical area referred to as the "MRF domain." Ultimately, the reliability of the rotational method, in conjunction with the findings from the meshing convergence analysis, was validated against experimental data. This validation was accomplished by estimating the forces exerted by the propeller at different rotational velocities, and the results of this validation are presented in Section 3.

The case corresponding to Figure 4b, is used to study the effect of fixed and horizontal moving obstacle proximity on the propeller performance. Thus, the distance from the propeller to the obstacle was progressively reduced from 1 m to 0.1 m and the effect was evaluated at different rotational velocities (3000 rpm, 5000 rpm, 9550 rpm). These rotational values correspond to 25%, 52%, and 80% the maximum rotational speed of the drone motors, respectively. They represent a range of performance working points, that generate different thrust forces on the propeller to better study the interaction of the downwash with the obstacle. Furthermore, in the context of our project Deliv'Air, where the drone is required to approach buses or trams at low altitudes, the ability to operate at low rotational speeds is crucial. The variation in rotational speeds provides better predictions for power consumption under specific conditions, contributing to more effective battery management for the drone. Then, the effect of the moving wall on the propeller was studied with different horizontal moving velocities. The obstacle height was constant at 0.2 m, the velocity of the wall was constant at different values (5 m/s, 10 m/s, 15 m/s, and 20 m/s), and the rotational velocity of the propeller was also evaluated at different values (3000 rpm, 5000 rpm, 9550 rpm). It is important to note that the 0.2 m obstacle altitude was chosen as a reference point just before the UAV touches down during hovering or landing.

All simulations were executed in parallel on a computing system featuring Intel(R) Xeon(R) Silver 4214 CPUs, each with a 2.40 GHz processor, and equipped with a substantial 128 gigabytes of RAM. The chosen software for conducting these simulations was ANSYS 22.2, a commercial application. It's worth noting that all the methodologies were carried out in a steady-state manner, ensuring consistency and stability in the calculations. Besides, all the results regarding the thrust and power coefficient are averaged around 2 to 3% in case of oscillations and uncertainties during convergence. Averaging the data helps smooth out any fluctuations or uncertainties that may arise during the simulations, enhancing the reliability and accuracy of our findings.

2.3 | Partition of the fluid field

As depicted in Figure 5, the geometry encompasses the Phantom DJI 3 propeller, characterized by a diameter of 240 mm. It is important to note that the simulated fluid domain does not incorporate the solid part of the propeller. The overall domain was subdivided into three distinct regions:

- Rotational fluid zone (MRF domain): This area corresponds to the region where the propeller rotation is simulated. It represents the immediate vicinity of the propeller and its associated airflow.
- Refining zone: Surrounding the rotational fluid zone, this region is designated for refining the mesh and enhancing resolution, particularly in the vicinity of the propeller.
- Entire fluid field: This encompasses the entire fluid domain under consideration for the simulations.

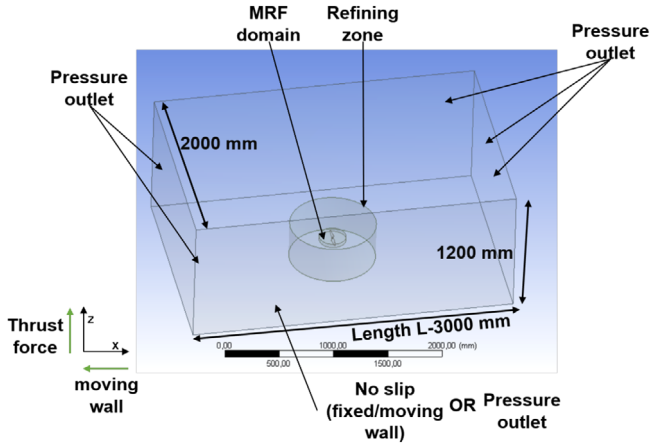

FIGURE 5 Geometrical model of the whole fluid domain, refining zone, and MRF fluid zone.

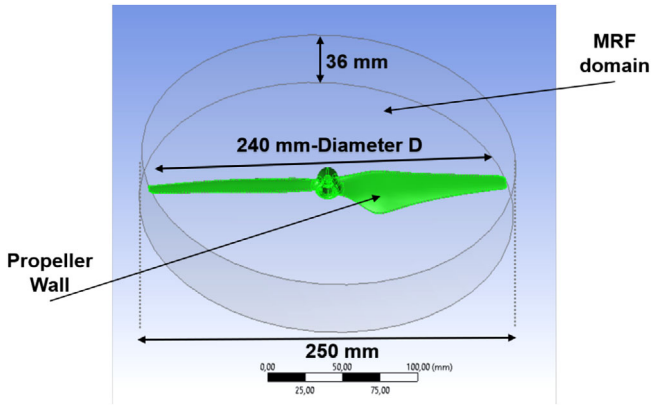

FIGURE 6 Moving Reference Frame (MRF) fluid domain.

Additionally, the figure provides comprehensive details regarding the dimensions and boundary conditions that were applied throughout the simulations. These dimensions and conditions play a critical role in accurately modeling and analyzing the flow dynamics around the propeller.

Figure 6 provides a visual representation of the propeller wall, the rotating MRF domain, and their respective dimensions. To accommodate the propeller's maximum diameter, denoted as D, and account for the simulated space, the overall wind field was defined as a rectangular domain with dimensions measuring 12.5 times D in length, 5 times D in height, and 8.3 times D in width.

The division of the fluid domain was accomplished using the design modeler within the ANSYS software package, while the meshes were generated utilizing ANSYS CFD meshing tools. Figure 5 provides a visual representation of the meshing and boundary conditions applied during the simulation.

For the walls encompassing the outer domain, boundary conditions were established as follows:

- Pressure outlet conditions were applied.

  Regarding the wall positioned beneath the propeller, the choice of boundary condition depended on the specific methodology employed in the simulation. It could be either:
  - A no-slip wall condition, signifying that the surface of the wall is stationary and the fluid in contact with it adheres without slipping.
  - A pressure outlet condition, depending on the simulation methodology chosen.

These boundary conditions play a crucial role in defining how the fluid interacts with the surfaces within the domain and are essential for accurately simulating the flow dynamics in the given configuration.

2.4 | Fluid dynamics analysis

Fluid Dynamics is a branch of physics, specifically, fluid mechanics which aims to study the behavior of fluids, liquids, and gases. Moreover, it has several domains, including aerodynamics and hydrodynamics [31]. Computational Fluid Dynamics (CFD) is a numerical method that replaced the analytical one due to the complexity of the Navier-Stokes equations by offering different models qualified for different cases over various types of problems and also depending on the capacity of the hardware. This section presents the numerical model used in this study to accurately predict the aerodynamic performance of the propeller.

2.4.1 | Conservation laws

In this study, we employ Equations (1) and (2) to address the fluid dynamics problem by applying the principles of mass and momentum conservation [32].

- Mass continuity (Conservation of mass)

$$\frac{\partial \rho}{\partial t} + \left(\rho u_j\right)_{,j} = 0. \tag{1}$$

- Conservation of momentum

$$\frac{\partial \rho u_i}{\partial t} + \left(\rho u_i u_j + p\delta_{ij}\right)_{,j} = \rho f_i + \tau_{ij,j}, \tag{2}$$

where ρ, u, and p are the density, the velocity components, and the pressure of the fluid, respectively, τ_{ij} the viscous stress, f_i the external body or volume forces, and t corresponds to time [32]. For a Stocks-Newtonian fluid, the term of the viscous stress τ_{ij} can be expressed as follows:

$$\tau_{ij} = \underbrace{\mu\left(\frac{\partial u_i}{\partial x_j} + \frac{\partial u_j}{\partial x_i}\right)}_{\text{Incompressible part}} - \underbrace{\frac{2}{3}\mu\frac{\partial u_k}{\partial x_k}\delta_{ij}}_{\text{Compressible part}}, \tag{3}$$

where μ is the dynamic viscosity of the fluid, and δ_{ij} is the Kronecker delta.

2.4.2 | Reynolds-averaged Navier-Stokes turbulence model (RANS)

Reynolds-Averaged Navier-Stokes equations are primarily used to describe turbulent flows. Moreover, RANS will be used in the simulations thanks to this model's advantages. RANS equations can solve the mean flow and can model the turbulent scales. Besides, 2D-3D numerical simulations can be performed with the lowest cost of calculations.

The Reynolds-Averaged Navier-Stokes equation is presented in Equation (4). Due to the Reynolds average process, an additional term arises which is the Reynolds-Stress [33]. The Reynolds-Stress is the product of two fluctuating velocity components averaged which is an unknown term in the Reynolds equation (4).

$$\frac{\partial(\rho \boldsymbol{U})}{\partial t} + \nabla \cdot (\rho \boldsymbol{U}\boldsymbol{U}) = -\nabla p + \nabla \cdot \left[\mu\left(\nabla \boldsymbol{U} + (\nabla \boldsymbol{U})^T\right)\right] + \rho \boldsymbol{g} \boldsymbol{f} - \nabla\left(\frac{2}{3}\mu(\nabla \cdot \boldsymbol{U})\right) - \nabla \cdot \underbrace{\left(\overline{\rho \boldsymbol{U}' \boldsymbol{U}'}\right)}_{\text{Reynolds-stress}}. \quad (4)$$

In order to solve the equation and close the problem, a model for the Reynolds Stress must be introduced in terms of quantities that are known. See Equation (5), where the model of the Reynolds Stress is presented. This model is the common approach for the Boussinesq hypothesis, where the mean velocity gradients are related to the dynamic turbulent viscosity μ_t [34].

$$\underbrace{-\overline{\rho \boldsymbol{U}' \boldsymbol{U}'}}_{\text{Reynolds stress}} = \mu_t \underbrace{\left(\nabla \boldsymbol{U} + (\nabla \boldsymbol{U})^T\right)}_{\text{Mean Velocity Gradients}} - \frac{2}{3}\rho k \boldsymbol{I} - \frac{2}{3}(\nabla \cdot \boldsymbol{U})\boldsymbol{I}, \quad (5)$$

where k is the turbulent kinetic energy and $\boldsymbol{I}$ is the identity matrix.

2.4.3 | Realizable and standard $k-\varepsilon$ models

When the Boussinesq hypothesis is made, the only remaining unknown term is the dynamic turbulent viscosity μ_t. This is when the $k-\varepsilon$ model comes to close and solves the problem by introducing the two terms: The turbulent kinetic energy k and the dissipation ϵ.

In Equation (6), the dynamic turbulent viscosity μ_t is presented in terms of k and ϵ. By having μ_t, the Reynolds Navier-Stocks equation can be closed and solved.

$$\mu_t = \rho C_\mu \frac{k^2}{\epsilon}. \quad (6)$$

An old way to calculate the Eddy viscosity term is by the mixing length models (L_m) and its updated version, the Van Driest mixing model. In these models, the mixing length was fixed and specified algebraically, hence the need to solve a transport equation instead.

Besides, the transport equation for k is presented in Equation (7). This equation is the same for the realizable and the standard $k-\varepsilon$ models.

$$\underbrace{\frac{\partial(\rho k)}{\partial t}}_{\text{Time}} + \underbrace{\nabla \cdot (\rho \boldsymbol{U} k)}_{\text{Convection}} = \underbrace{\nabla \cdot \left[\left(\mu + \frac{\mu_t}{\sigma_k}\right)\nabla k\right]}_{\text{Diffusion}} + \underbrace{P_k + P_b - \rho\epsilon + S_k}_{\text{Sources + Sinks}}, \quad (7)$$

where σ_k is the turbulent Prandtl number, P_k is the production due to mean velocity gradients, P_b is the production due to buoyancy, and S_k is a user-defined source [35].

Besides, the transport equation for ϵ is presented in Equation (8).

$$\underbrace{\frac{\partial(\rho \epsilon)}{\partial t}}_{\text{Time}} + \underbrace{\nabla \cdot (\rho \boldsymbol{U} \epsilon)}_{\text{Convection}} = \underbrace{\nabla \cdot \left[\left(\mu + \frac{\mu_t}{\sigma_\epsilon}\right)\nabla \epsilon\right]}_{\text{Diffusion}} + \underbrace{C_1 \frac{\epsilon}{k}(P_k + C_3 P_b) - C_2 \rho \frac{\epsilon^2}{k} + S_\epsilon}_{\text{Sources + Sinks}}. \quad (8)$$

This equation is similar to Equation (7) in terms of convection, diffusion, source, and sinks terms. However, in the sources and sinks terms, the empirical model coefficients C_1, C_2, and C_3 are presented. These empirical model coefficients will vary depending on the $k-\varepsilon$ models (standard or realizable).

2.4.4 | $k-\omega$ shear stress transport (SST) model

$k-\varepsilon$ model is best suited for flow away from the wall. However, the $k-\omega$ model is best suited for flow near the wall. The SST model is a combination of $k-\omega$ and $k-\varepsilon$. Besides, in the $k-\omega$ model, the wall shear stress is too high and the flow does not separate from the smooth surfaces. Hence, the $k-\omega$ SST model attempts to address and solve these problems and give better separation prediction.

The standard $k-\varepsilon$ model is presented in Equations (9) and (10).

$$\frac{\partial(\rho k)}{\partial t} + \nabla \cdot (\rho \boldsymbol{U} k) = \nabla \cdot \left(\left(\mu + \frac{\mu_t}{\sigma_k}\right)\nabla k\right) + P_k - \rho\epsilon, \quad (9)$$

$$\frac{\partial(\rho \epsilon)}{\partial t} + \nabla \cdot (\rho \boldsymbol{U} \epsilon) = \nabla \cdot \left(\left(\mu + \frac{\mu_t}{\sigma_\epsilon}\right)\nabla \epsilon\right) + C_{1\epsilon} P_k \frac{\epsilon}{k} - C_{2\epsilon}\rho \frac{\epsilon^2}{k}, \quad (10)$$

with,

$$\epsilon = C_\mu k\omega. \tag{11}$$

By substituting $\epsilon = C_\mu k\omega$ in Equations (9) and (10) we obtain Equation (12) below.

$$\frac{\partial(\rho\omega)}{\partial t} + \nabla\cdot(\rho \boldsymbol{U}\omega) = \nabla\cdot\left(\left(\mu + \frac{\mu_t}{\sigma_k}\right)\nabla\omega\right) + \frac{\gamma}{\nu_t}P_k - \beta\rho\omega^2 + \underbrace{2\frac{\rho\sigma_{\omega 2}}{\omega}\nabla k : \nabla\omega}_{\text{Additional Term}}, \tag{12}$$

where γ and β are constants, σ_{ω^2} is the turbulent Prandtl number for ω, ω is the specific dissipation rate, and Δk and $\Delta\omega$ are the gradients of turbulent kinetic energy and specific dissipation rate, respectively.

The $k-\omega$ model equation is presented below in Equation (13).

$$\frac{\partial(\rho\omega)}{\partial t} + \nabla\cdot(\rho \boldsymbol{U}\omega) = \nabla\cdot\left(\left(\mu + \frac{\mu_t}{\sigma_k}\right)\nabla\omega\right) + \frac{\gamma}{\nu_t}P_k - \beta\rho\omega^2. \tag{13}$$

Comparing Equations (12) and (13), all the terms are identical except the additional term.

Moreover, the additional term that exits in the $k-\omega$ model is presented below in Equation (14).

$$2\frac{\rho\sigma_{\omega 2}}{\omega}\nabla k : \nabla\omega. \tag{14}$$

This term appears in some turbulence models and represents the effect of the anisotropy of the Reynolds stress on the specific dissipation rate. Multiplying this term by $(1-F_1)$, we obtain the Equation (15) presented below.

$$2(1-F_1)\frac{\rho\sigma_{\omega 2}}{\omega}\nabla k : \nabla\omega, \tag{15}$$

where F_1 is a blending function, depends on the local flow conditions, and is typically determined from empirical data depending on the turbulence model used.

By merging the $k-\varepsilon$ and $k-\omega$ models, the $k-\omega$ shear stress transport (SST) turbulence model has demonstrated its effectiveness in anticipating wall-induced flow separation, achieving results that closely resemble experimental data when compared to alternative turbulence models, as discussed in [36]. Consequently, we employed the $k-\omega$ SST model in this study to simulate the downwash flow generated by the propeller.

3 | MESH AND PROPELLER ROTATIONAL MODEL VALIDATION

To build upon and bolster our earlier studies [27, 37, 38], mesh independence and convergence studies were performed for this computational model using the methodology presented in Figure 4a. The tests included five variants, as they allowed one to capture the trend and draw conclusions. Besides, the mesh independence study was performed for the rotating propeller domain (more dense mesh in this area), the refining zone, and the whole outer domain, and the quality of the mesh was verified for the overall domain in eleven different mesh cases (see Figure 7 and Table 1). The performance of the mesh was assessed by means of the power and thrust coefficient on the propeller, expressed by.

$$C_T = \frac{T}{\rho n^2 D^4}, \tag{16}$$

$$C_P = \frac{P}{\rho n^3 D^5}, \tag{17}$$

where T represents the thrust force, P corresponds to the power derived from torque, ρ denotes fluid density, n signifies rotational velocity, and D stands for the propeller's diameter.

The total number of elements varied from 500000 to 18 million, as the number of elements along the blade span and blade chord was changed. The sizing of the first layer varied from 7×10^{-4} m to 5×10^{-6} m. This represents the minimum size of the first layer around the propeller wall which was refined from mesh refinement 1 (7×10^{-4} m) to mech refinement 11 (5×10^{-6} m). Finally, several criteria were also checked to obtain good mesh quality. The results of the study showed that the difference between observed parameters for the least and the densest meshes were 2,8% and 1,8% for the thrust and power coefficient, respectively. As shown in Table 1, the last five mesh cases (7, 8, 9, 10, and 11) are independent of the five variants with less than 0.8% difference (CT and CP comparison with the precedent value). Consequently, the mesh with the lowest number of elements (between the last five meshes) was chosen. Attempts to further increase the mesh size resulted in the same mesh quality and performance; therefore, mesh case number 7 was used in this study to reduce the computational cost. Finally, using this mesh refinement, the thrust and power coefficients are also close to the values obtained in the experimental tests just presented below [5].

Considering efficiency and the relatively small dimensions of the propeller, an unstructured tetrahedral element was adopted. The resultant meshes are depicted in Figure 8, with a total of 922,359 nodes and 5,222,363 elements.

In order to confirm the effectiveness of the mesh and rotation approach outlined in this paper for replicating propeller rotation, a series of simulations were conducted to reproduce experiments detailed in the work of Deters and Kleinke [5]. The experimental procedure involved the use of an isolated

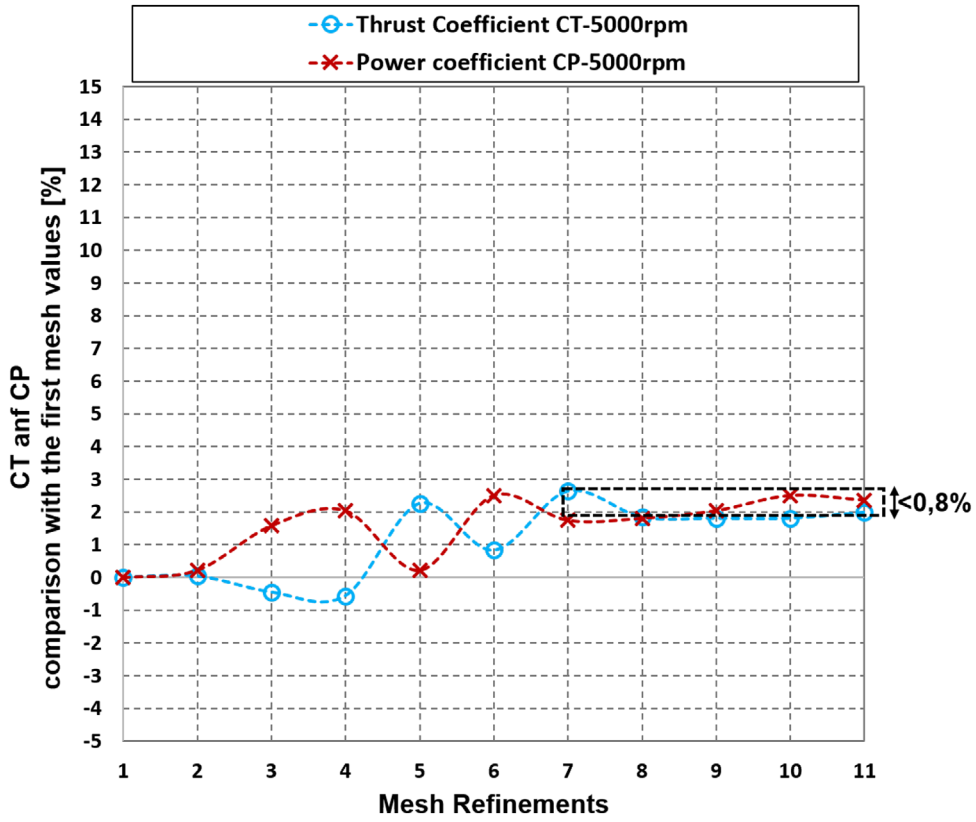

FIGURE 7 Mech Convergence study on the power and thrust coefficient.

TABLE 1 Eleven mesh refinement densities with 5 variants and comparison (aspect ratio, orthogonal quality, nodes, elements, layer min size on the propeller wall).

Mesh Refinements	1	2	3	4	5	6	7	8	9	10	11
Aspect ratio	1.8774	1.8744	1.8666	1.8557	1.8567	1.8389	**1.8291**	1.8238	1.8163	1.8096	1.7997
Orthogonal Quality	0.75919	0.76005	0.76214	0.76521	0.76347	0.77029	**0.77485**	0.77753	0.78111	0.78432	0.78901
Nodes	88982	105504	129589	170399	234853	659996	**922359**	1239582	1544490	1935155	3139715
Elements	503132	596483	732041	959801	1318618	3725509	**5222363**	7105940	8907978	11204252	18283210
Local Min Size[m] (propeller)	7.00E-04	6.00E-04	5.00E-04	4.00E-04	3.00E-04	1.00E-04	**1.00E-05**	1.00E-05	1.00E-05	1.00E-05	5.00E-06
Comparison CP[%] (to precedent value)	0.0	0.2	1.4	0.5	−1.8	2.3	**−0.7**	0.1	0.2	−0.5	0.1
Comparison CP[%] (to precedent value)	0.0	0.0	−0.5	−0.1	2.8	−1.4	**1.8**	−0.8	0.0	0.0	0.2

Phantom DJI 3 propeller powered by an electric motor, mounted on a balance to measure both thrust and torque. Various rotational velocities were applied to the propeller, and the results were presented in terms of the previously defined thrust and power coefficients.

In terms of the CFD simulations, the Phantom DJI 3 propeller was assessed at six distinct rotational speeds falling within the range covered by the experiments, as illustrated in Figure 9. The CFD outcomes for the thrust coefficient (C_T) and the power coefficient (C_P) are represented in the plot as red diamonds and green plus signs, respectively. These results exhibit favorable concordance with the experimental findings reported by Deters and Kleinke [5] and with the CFD results from Paz et al [17].

The CFD findings in this research tend to underestimate the thrust coefficient when the rotational velocity exceeds 3000 rpm. Nevertheless, this underestimation remains below 8% when compared to the experimental data from [5]. Moreover, the CFD outcomes in this paper align closely with the curves of both the experimental data and the CFD results presented in

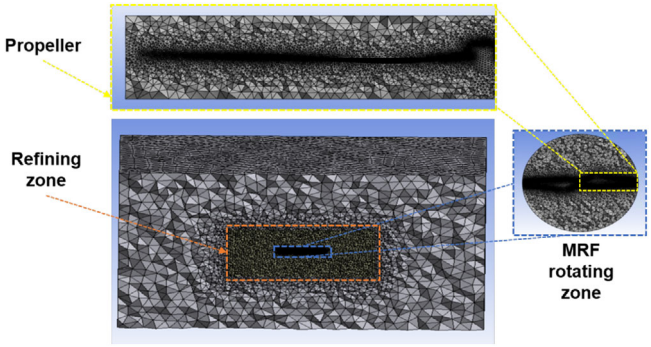

FIGURE 8 Elements of the entire, refining, and propeller fluid domains.

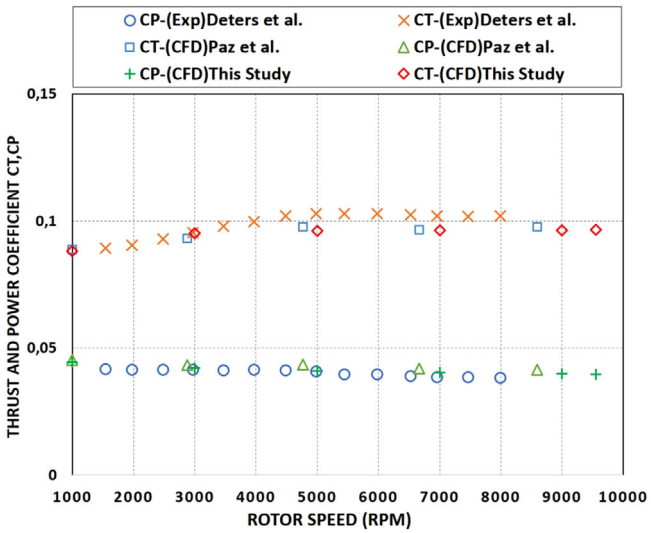

FIGURE 9 Validation of the rotation propeller methodology.

Paz et al [17]. Consequently, the rotation methodology and mesh performance employed in this study are deemed appropriate for replicating the reaction force experienced by the propeller during airflow generation.

4 | RESULTS AND DISCUSSION

4.1 | Fixed obstacle effect on the propeller

Following the validation of the mesh and the numerical method, the study proceeded to examine the propeller's response to its proximity to an obstacle. To accomplish this, simulations were conducted introducing a solid wall beneath the propeller at varying distances, applying the methodology (b) as previously detailed in Figure 4. Corresponding adjustments were made to the boundary conditions, and simulations were executed at different rotational velocities, namely 3000 rpm, 5000 rpm, and 9550 rpm.

Additionally, the simulations at the three different rotational velocities were subjected to comparison with the CFD results from Paz et al [17] and with the mathematical model derived

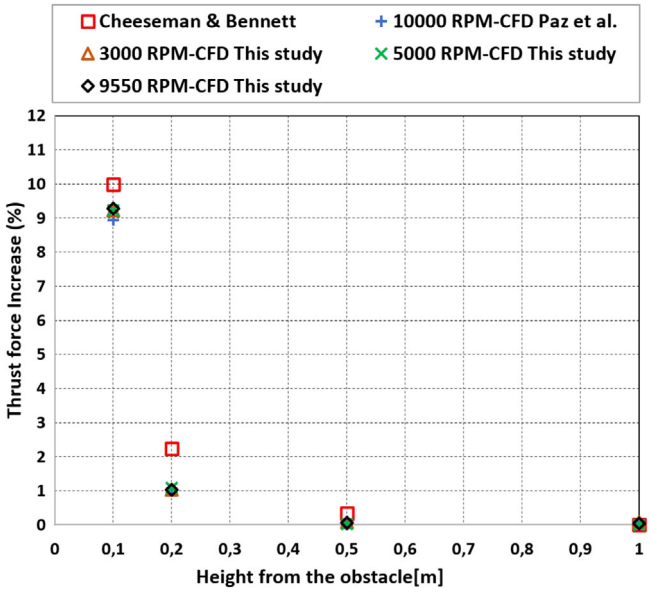

FIGURE 10 Effect of fixed obstacle proximity on an isolated propeller.

from the method of images, as presented by Cheeseman and Bennett [7].

$$\frac{T}{T_\infty} = \frac{1}{1 - \left(\frac{R}{4z}\right)^2}, \tag{18}$$

where R signifies the propeller's radius, z represents the vertical separation from the obstacle, T denotes the thrust produced by the propeller when influenced by the obstacle, and T_∞ indicates the propeller's thrust when not affected by the obstacle. The incorporation of these three velocity scenarios in the simulations enables the assessment of the applicability of the CFD methodology and the theoretical model across a wide range of rotational speeds. Furthermore, this comparison between CFD results and other theoretical and CFD data reinforces the validation of both the mesh performance and the methodology applied in this study.

The outcomes are visually presented in Figure 10, illustrating the variation in thrust force at various distances from the obstacle and across different rotational speeds (3000 rpm, 5000 rpm, and 9550 rpm). The thrust force increase percentage is computed by employing the formula $(T\text{-}T_\infty)/T_\infty$.

The results derived from Cheeseman and Bennett's theoretical model are represented as red squares. Furthermore, the CFD simulations conducted in this study, as well as the CFD simulations performed by Paz et al., and the theoretical data, all closely adhere to the same curve. However, both CFD results exhibit a slight underestimation, approximately 1% lower than the actual thrust generated by the propeller at distances of 0.1 m and 0.2 m from the obstacle.

Additionally, Figure 11 showcases the velocity fields of the propeller operating at 3000 rpm, 5000 rpm, and 9550 rpm in the presence of the obstacle. This is compared to the "no-ground effect" condition (labeled as 'a'). The fluid tube generated by

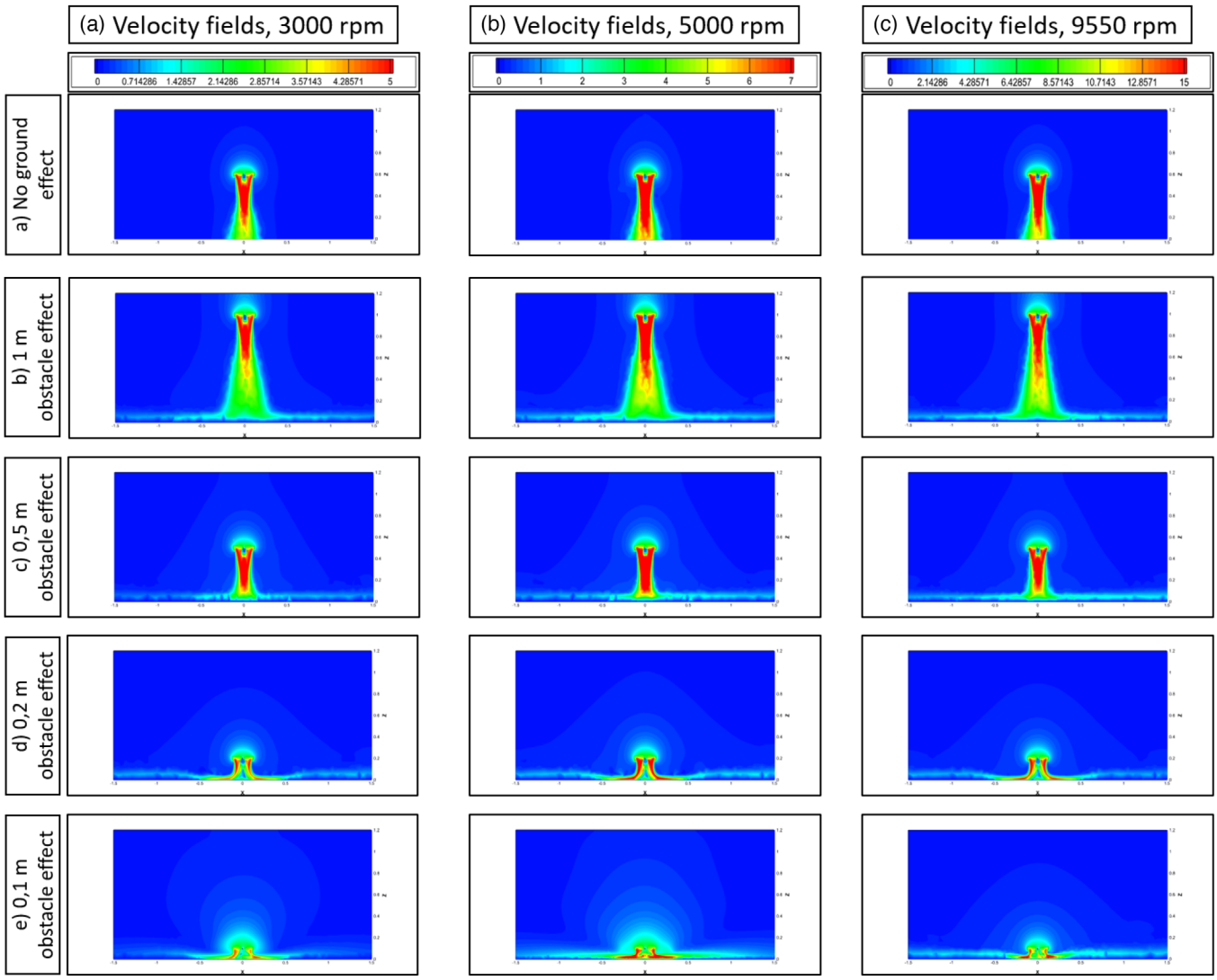

FIGURE 11 Velocity fields of an isolated propeller (3000, 5000, and 9550 rpm), at different obstacle heights (no ground, 1 m, 0.5 m, 0.2 m, 0.1 m).

the propeller in the 'no-ground effect' condition demonstrates an unobstructed, symmetrical, and rectilinear downward flow trajectory. All velocity fields are illustrated in the xz-plane. The x-axis is employed to depict contours in the x-direction, providing a clearer insight into the behavior of the moving wall. Simultaneously, the z-axis displays contours in the z-direction and serves as a reference for tracking the thrust force exerted on the propeller. The xz-plane is taken in the middle of the whole domain crossing the propeller.

The cause behind the increase in propeller thrust observed at distances of 0.1 m and 0.2 m from the obstacle is elucidated in Figure 11, specifically in panels (d) and (e) for the three different rotational speeds. The obstacle's close proximity to the propeller induces a radial deviation in the flow tube, resulting in a thrust increase. Conversely, when the obstacle is positioned farther from the propeller, the flow remains unaffected by the ground, and there is no deviation, as illustrated in the images corresponding to cases (b) and (c).

4.2 | Moving obstacle effect on the propeller (3000 rpm)

The final phase of this study involved an assessment of the impact of a moving obstacle on a propeller hovering at three different rotational speeds: 3000 rpm, 5000 rpm, and 9550 rpm, all at a distance of 0.2 m from the obstacle. This scenario emulates a drone hovering at a specific altitude, awaiting the approach of a moving vehicle such as a train, bus, or car. It's important to note that this specific study focuses exclusively on the hovering phase above the moving obstacle and does not address the approach or departure phases.

In these CFD simulations, the moving obstacle's horizontal velocities were investigated, with the results compared to a reference case involving a fixed obstacle that caused a 1% thrust effect on the propeller. The variations in thrust force for the propeller hovering at 3000 rpm are presented in Figure 12. The findings reveal an initial 1.92% increase in the lift for moving

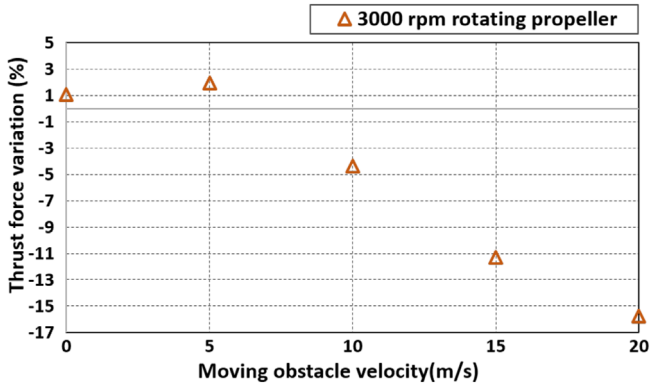

FIGURE 12 Effect of moving obstacle proximity (0.2 m) on the propeller thrust (3000 rpm).

obstacles at 5 m/s, followed by a subsequent decrease of 4.4%, 11.3%, and 15.8% for obstacle speeds of 10 m/s, 15 m/s, and 20 m/s, respectively, in comparison to the thrust generated when no obstacle is present (0 m/s).

The underlying cause of the thrust variation in close proximity to a moving obstacle is visually explained in Figure 13, particularly in panels (a) and (b), offering a detailed depiction of the velocity fields associated with the propeller rotating at 3000 rpm. In Figure 13a, you can observe the flow over the obstacle moving in the (x) direction at 5 m/s, along with the downwash generated by the propeller, propagating in both the (x) and (-x) directions. These flow patterns interact with each other on the left side of the downwash, creating a minor separation zone at a distance away from the propeller ($x = -0.5$ m), consequently leading to thrust variation. Additionally, the robust interaction between the downwash and the flow produced by the moving obstacle contributes to an increase in thrust.

Figure 13b displays the flow characteristics over the obstacle as it moves in the (x) direction at 10 m/s, accompanied by the downwash generated by the propeller, propagating in both the (x) and (-x) directions. These flows exhibit a modest interaction on the left side of the downwash, resulting in a substantial separation zone adjacent to the propeller. This substantial separation zone is responsible for a notable decrease in thrust, amounting to a 4.4% reduction.

Figure 13c shows the flow over the obstacle moving along (x) direction at 15 m/s, and the downwash of the propeller generated in both the positive and negative x-directions. The flows slightly interfere with each other on the left side of the downwash, resulting in a large separation zone next to the propeller. This causes a significant decrease in thrust by 11.3%.

Figure 13d illustrates the effect of an obstacle moving at a velocity of 20 m/s in the x-direction on the flow of a propeller rotating at 3000 rpm. The downwash generated by the propeller creates a zone of interference on the left side, leading to a severe separation zone that causes a decrease of 15.8% in the thrust.

The reduction in thrust force experienced by the propeller while hovering at distances of 0.2 m from a moving wall at velocities of 10 m/s, 15 m/s, and 20 m/s can be attributed to the visible separation of the downwash, specifically evident on

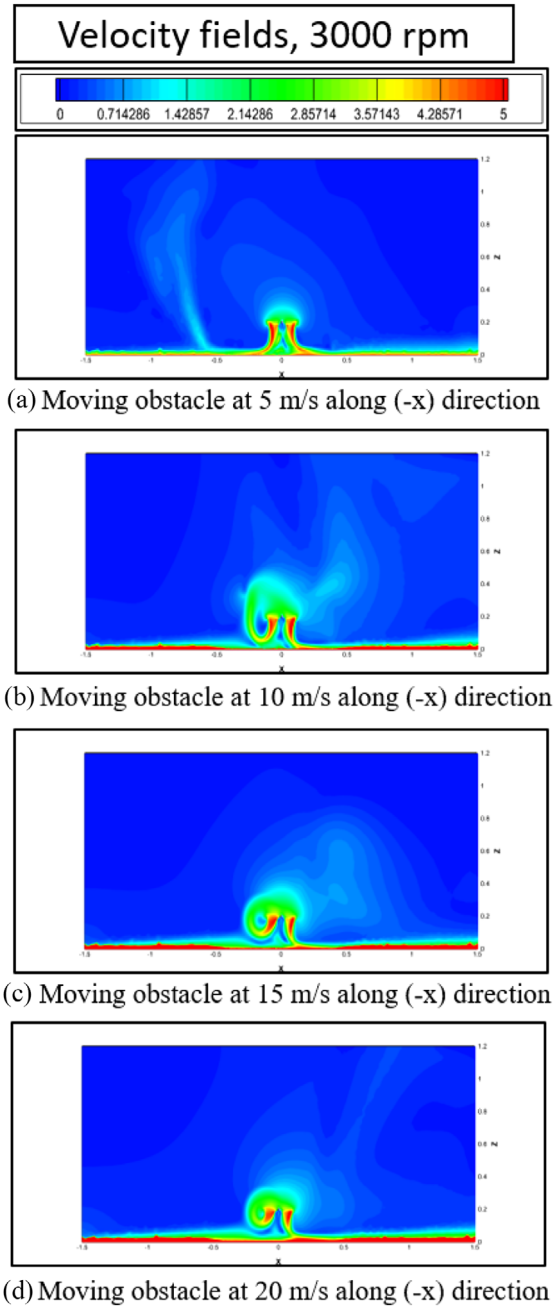

FIGURE 13 Velocity fields, effect of moving obstacle proximity (0.2 m) on the propeller (3000 rpm): (a) moving obstacle at 5 m/s along (-x) direction, (b) moving obstacle at 10 m/s along (-x) direction, (c) moving obstacle at 15 m/s along (-x) direction, (d) moving obstacle at 20 m/s along (-x) direction.

the left side of the propeller, as depicted in the velocity fields Figure 13b–d. This separation phenomenon arises due to the movement of the wall in the (-x) direction, generating a high-pressure zone on the right side and a low-pressure zone on the left side. This pressure differential creates an aspiration zone, forcing the propeller to lose thrust. An alternative interpretation emphasizes that the separation zone expands progressively with increasing wall velocity. The turbulent wake, observable in the velocity fields at 10 m/s, 15 m/s, and 20 m/s, is then drawn towards the propeller, creating a high-pressure zone above it and

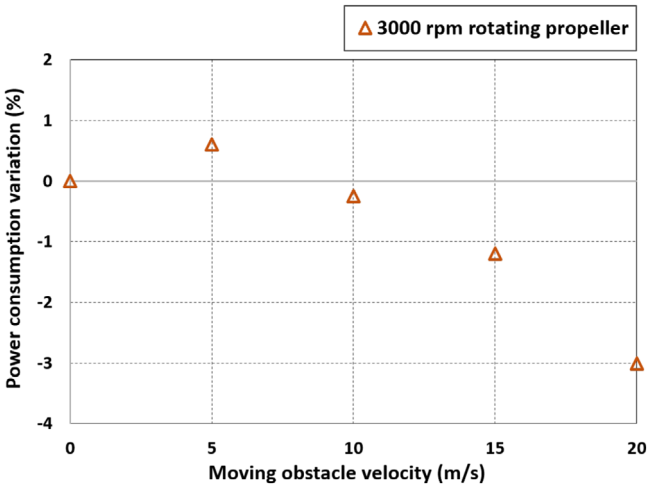

FIGURE 14 Effect of moving obstacle proximity (0.2 m) on the propeller power consumption (3000 rpm).

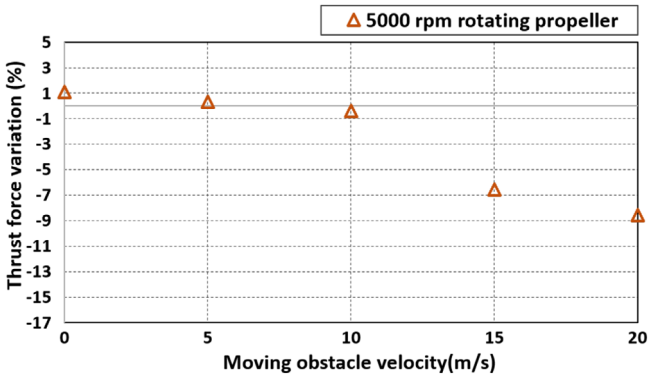

FIGURE 15 Effect of moving obstacle proximity (0.2m) on the propeller thrust (5000 rpm).

inducing a decrease in thrust. To counteract this turbulent and unstable loop, the propeller must augment its rotational speed, subsequently increasing its thrust to maintain both altitude and overall power loading. It is crucial to note that this adjustment in rotational speed also impacts the battery energy, as discussed earlier and in other studies [27].

Moreover, when hovering above a moving obstacle at 3000 rpm, the perturbations and the huge decrease in the thrust force at high horizontal moving velocities cause a slight drop in the power consumption of the propeller. The effect of the moving wall on the variation of the power consumption is illustrated in Figure 14. A slight increase in the power is noticed when the obstacle is moving at 5 m/s; however, the power drops progressively by 1.2%, and 3% when the obstacle is moving at 15 m/s and 20 m/s, respectively. The power consumption is predicted using the CFD simulations based on the torque and the rotational speed of the propeller.

4.3 | Moving obstacle effect on the propeller (5000 rpm)

A parametric exploration was conducted to examine the aerodynamic performance of the propeller when exposed to a moving wall at 5000 rpm. CFD simulations were executed, encompassing four distinct horizontal velocities for the wall, while the reference case consisted of a fixed obstacle causing a 1% thrust effect on the propeller. The thrust force variations for the propeller hovering at 5000 rpm are presented in Figure 15. The findings reveal a gradual reduction in lift by 0.33%, 0.37%, 6.55%, and 8.55% for moving obstacles at velocities of 5 m/s, 10 m/s, 15 m/s, and 20 m/s, respectively, compared to the thrust generated by a fixed wall (which causes a 1% thrust effect at 0 m/s). It is worth noting that the influence of moving walls at low velocities on thrust is nearly imperceptible when the propeller is hovering at 5000 rpm. However, the thrust is still impacted when the wall is in motion at higher speeds.

The underlying cause of the thrust variation near a moving obstacle is elucidated in Figure 16, with a detailed presentation of the velocity fields related to the propeller's operation at 5000 rpm, showcased in panels (a) and (b). In Figure 16a, you can observe the flow pattern over the obstacle as it moves in the (x) direction at 5 m/s, along with the downwash generated by the propeller, propagating in both the (x) and (-x) directions. These flow patterns interact on the left side of the downwash, creating a small separation zone at a distance from the propeller ($x = -1$ m), which leads to thrust variation. Furthermore, the strong interaction between the downwash and the flow generated by the moving obstacle causes a relatively minor fluctuation in thrust. Additionally, it's evident that the downwash separation is gradually moving farther from the propeller in comparison to the hovering speed of 3000 rpm.

In Figure 16b, the flow dynamics over the obstacle are displayed as it moves in the (x) direction at 10 m/s. Concurrently, the downwash generated by the propeller extends in both the (x) and (-x) directions. These flow patterns exhibit slight interference on the left side of the downwash, resulting in the formation of a substantial separation zone near the propeller. This separation zone leads to a reduction in thrust, amounting to a decrease of 0.37%.

In Figure 16c, the flow dynamics are depicted over the obstacle moving in the (x) direction at a speed of 15 m/s, accompanied by the downwash generated by the propeller, extending in both the positive and negative x-directions. These flow patterns exhibit a modest degree of interference on the left side of the downwash, giving rise to a considerable separation zone adjacent to the propeller. This separation zone results in a noteworthy reduction in thrust, amounting to a 6.55% decrease.

Figure 16d illustrates the effect of an obstacle moving at a velocity of 20 m/s in the x-direction on the flow of a propeller rotating at 5000 rpm. The downwash generated by the propeller creates a zone of interference on the left side, leading to a severe separation zone that causes a decrease of 8.55% in the thrust.

Regarding the power consumption of the propeller, a slight decrease by 1.78% is noticed when the obstacle is moving at 20 m/s. The effect on the thrust and the power consumption is negligible at low moving wall speeds due to the increase in the hovering velocity.

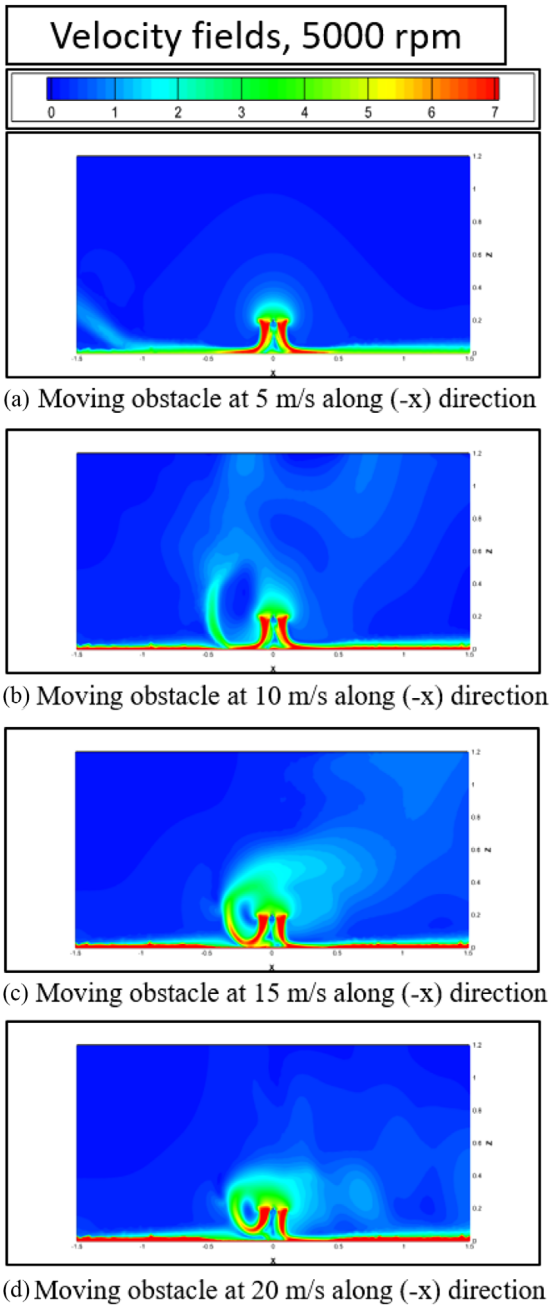

FIGURE 16 Velocity fields, effect of moving obstacle proximity (0.2 m) on the propeller (5000 rpm): (a) moving obstacle at 5 m/s along (-x) direction, (b) moving obstacle at 10 m/s along (-x) direction, (c) moving obstacle at 15 m/s along (-x) direction, (d) moving obstacle at 20 m/s along (-x) direction.

4.4 | Moving obstacle effect on the propeller (9550 rpm)

The thrust force variation on the propeller hovering at 9550 rpm is shown in Figure 17. The results have shown an inconsiderable decrease in the lift by 0.11% for 5 m/s, 10 m/s, 15 m/s, and by 0.9% for 20 m/s moving obstacle, compared to fixed wall thrust (1% at 0 m/s). It is noticeable that the effect of moving walls at low and high velocities on the thrust is almost negligible when the propeller is hovering at 9550 rpm.

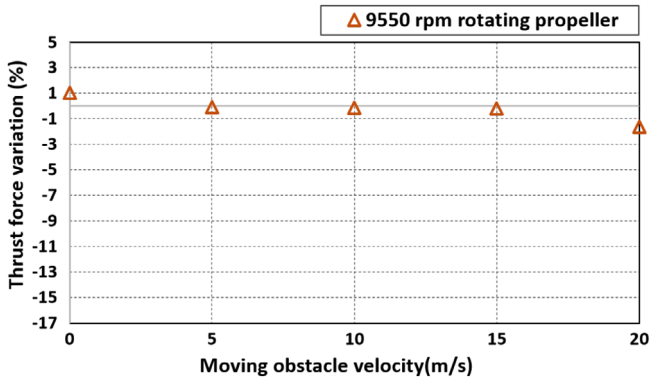

FIGURE 17 Effect of moving obstacle proximity (0.2 m) on the propeller thrust (9550 rpm).

The underlying cause of the thrust variation near a moving obstacle is elucidated in Figure 18, with a comprehensive depiction of the velocity fields pertaining to the propeller's operation at 9550 rpm, as presented in panels (a) and (b). In Figure 18a, the flow pattern over the obstacle is showcased as it moves in the (x) direction at 5 m/s. Simultaneously, the downwash generated by the propeller extends in both the (x) and (-x) directions. These flow patterns exhibit interference on the left side of the downwash, leading to the emergence of a small separation zone located at a distance from the propeller ($x = -1.2$ m). This separation zone contributes to the thrust variation. Besides, the strong interference between the downwash and the flow generated by the moving obstacle causes an insignificant variation in the thrust. It is also visible that the downwash separation is moving further from the propeller compared to the hovering speeds of 3000 rpm and 5000 rpm. Thus, the confirmation that the rotational speed of the propeller is a favorable parameter to control the stability of the vehicle.

In Figure 18b, the flow dynamics are illustrated over the obstacle as it moves in the (x) direction at a velocity of 10 m/s. Simultaneously, the downwash generated by the propeller extends in both the (x) and (-x) directions. These flow patterns exhibit slight interference on the left side of the downwash, leading to the formation of a separation zone located at a distance of 0.9 m from the propeller. This separation zone induces a minimal variation in the thrust.

In Figure 18c, the illustration portrays the flow dynamics over the obstacle in motion along the (x) direction at a rate of 15 m/s. Concurrently, the downwash generated by the propeller extends in both the positive and negative (x) directions. These flow patterns exhibit a slight degree of interference on the left side of the downwash, giving rise to the formation of a separation zone adjacent to the propeller, specifically at the location of $x = -0.8$ m. This separation zone results in a minor decrease in the thrust.

Figure 18d illustrates the effect of an obstacle moving at a velocity of 20 m/s in the x-direction on the flow of a propeller rotating at 9550 rpm. The downwash generated by the propeller creates a zone of interference on the left side, leading to a separation zone that causes a decrease of 0.9% in the thrust.

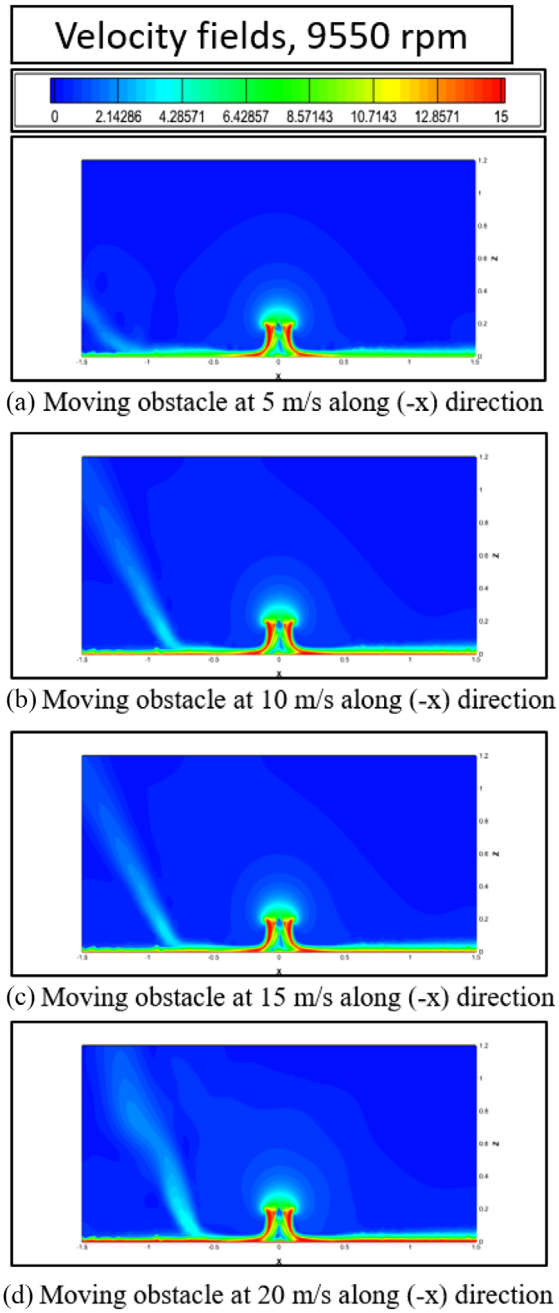

FIGURE 18 Velocity fields, effect of moving obstacle proximity (0.2 m) on the propeller (9550 rpm): (a) moving obstacle at 5 m/s along (-x) direction, (b) moving obstacle at 10 m/s along (-x) direction, (c) moving obstacle at 15 m/s along (-x) direction, (d) moving obstacle at 20 m/s along (-x) direction.

4.5 | Payload capabilities and hovering efficiency of the propeller

As presented in the previous parts, the aerodynamic performance of the propeller in low hovering conditions is strongly affected in the presence of horizontal moving walls at moderate and high speeds. Throughout this investigation, it is proved that increasing the rotational velocity of the rotor when facing severe variation in the thrust and the power, leads to stabilization and full control of the aerodynamic performance of the propeller

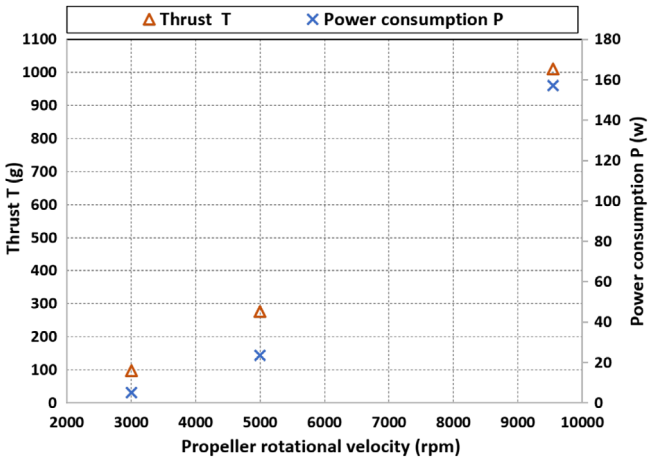

FIGURE 19 The evolution of the thrust and power consumption of the propeller (3000, 5000, 9550 rpm) in hovering at 0.2 m from the obstacle.

and hence the stability of the vehicle. However, the increase in the propeller rotational velocities increases the power consumption as well as the payload of the UAV. The payload of the phantom DJI 3 propeller studied in this research is presented along with the power consumption over the three rotational velocities in Figure 19.

If the propeller is hovering at 3000 rpm, this means that the maximum payload is 100 g and the power consumption is approximately 18.6 W. When hovering above a moving wall at 10 m/s, 15 m/s, or 20 m/s, it is preferred to increase the rotational velocity, leading to an increase in the thrust and the power consumption as presented in Figure 19. The increase in the thrust when controlling the rotational speed would fill the gap caused by the effect of the moving obstacle (a huge decrease in the thrust), leading to the stabilization of the propeller. However, this increase in the thrust and the payload leads to an increase in power consumption that can go up to 160 W (9550 rpm) compared to 3000 rpm. Besides, if the propeller is hovering at 5000 rpm, the effect of the moving walls is neglected at low speeds and rotor control must be ensured when facing high speeds obstacles.

In the context of thrust control, the CFD results derived from this study, specifically concerning the thrust increase when approaching a fixed wall or the decrease in thrust over a moving wall, offer valuable insights for refining and enhancing the control algorithm of the UAV. Drawing parallels with the work conducted by Mohammed Rabah et al. [39], who utilized CFD results to account for ground effects in their PID and Fuzzy Logic controllers, our study's findings contribute to the optimization of control methodologies when encountering obstacles such as fixed and moving walls. The outcomes obtained from our investigation, particularly regarding the impact of a moving wall on a propeller rotating at low rotational speed (3000 rpm), can now serve as instrumental data for fine-tuning and augmenting the capabilities of various controllers. This refinement is particularly relevant when the drone maneuvers in the presence of a moving wall, as anticipated in the Deliv'AIR project. This collaborative approach,

leveraging CFD insights, not only aligns with established practices, as demonstrated by Mohammed Rabah et al. [39], but also extends the applicability of such methodologies to dynamic scenarios, enhancing the UAV's performance and adaptability during real-world operations.

5 | CONCLUSIONS

This paper has provided an analysis of the aerodynamic performance of a Phantom DJI 3 propeller, taking into consideration the influence of stationary and moving obstacles. We conducted numerical simulations employing the commercially available CFD solver, Ansys FLUENT. The steady simulations, which were founded on the MRF model, have proven to be efficient. They demonstrate a robust replication of the flow generated by the propeller near moving obstacles, all while maintaining a reasonable computational cost and avoiding the associated expenses of physical experimentation. Our CFD simulations of a single propeller have exhibited a substantial correlation between changes in thrust and the various methodologies employed. This correlation is consistent across all altitudes, aligns well with other numerical and theoretical models, and remains reliable for a range of obstacle velocities. Consequently, the study exclusively focused on simulating the behavior of an isolated propeller within an environment featuring moving walls. The primary objective was to gain a deeper understanding of the complex interactions between the propeller's downwash and the delicate airflow patterns generated by these moving walls. This investigation served a dual purpose: firstly, to explain the isolated propeller's unique aerodynamic behavior, devoid of the influence of neighboring propellers, and secondly, to predict its behavior when it operates in the proximity of moving obstacles, particularly in the context of larger quadcopters where each propeller can be considered in isolation due to their significant spatial separation.

Numerical simulations were obtained with velocity field distributions at different obstacle altitudes (0.1 m, 0.2 m, 0.5 m, 1 m) and different obstacle horizontal velocities (5 m/s, 10 m/s, 15 m/s, 20 m/s) to describe the aerodynamic interference effect of a moving obstacle on the propeller. When hovering at 3000, 5000, and 9550 rpm, the results showed an increase in the lift force on the propeller by 9.3%, and 1.03% due to the presence of a fixed obstacle (wall) placed at 0.1 m and 0.2 m from the propeller, respectively. During hovering at 3000 rpm, at a distance of 0.2 m above a moving obstacle with speeds of 5 m/s, 10 m/s, 15 m/s, and 20 m/s, the findings revealed a 1.92% increase in lift for a 5 m/s moving obstacle. However, a significant reduction in lift was observed, amounting to 4.4%, 11.3%, and 15.8% for obstacle speeds of 10 m/s, 15 m/s, and 20 m/s, respectively. Similarly, during hovering at 5000 rpm and maintaining a distance of 0.2 m above a moving obstacle with speeds of 5 m/s, 10 m/s, 15 m/s, and 20 m/s, a gradual reduction in lift was observed. The reductions were 0.33%, 0.37%, 6.55%, and 8.55% for respective obstacle speeds compared to the thrust generated by a fixed wall. When hovering at 9550 rpm at a height of 0.2 m above a moving obstacle with speeds of 5 m/s, 10 m/s, 15 m/s, and 20 m/s, the results indicated minimal reductions in lift. These reductions amounted to 0.11% for speeds of 5 m/s, 10 m/s, and 15 m/s, and a slightly larger reduction of 0.9% for a 20 m/s moving obstacle, compared to the thrust generated by a fixed wall (set at 1% thrust at 0 m/s). As the velocity of the obstacle increases, the swirling flow and the separation zones dominate the flow field to the left of the propeller, causing severe variation in the thrust force, and the power consumption. Such a rapid shift in the propeller's performance could potentially result in destabilization, posing a risk of the vehicle's position deteriorating and colliding with the obstacle if the dynamic system (control techniques) fails to respond appropriately. However, as the rotational speed of the propeller increases, the impact of the moving obstacle on the vehicle's force parameters becomes insignificant. This is chiefly due to the increased distance between the separation zones and the downwash generated by the propeller.

In this regard, the results of the present paper lead to new concerns, proposing for future work the necessity of analyzing several cases with several propellers, which would guarantee the safety of the whole UAV in any possible flying scenarios near a moving obstacle.

AUTHOR CONTRIBUTIONS

Charbel Hage: Conceptualization; data curation; formal analysis; investigation; methodology; software; validation; visualization; writing—original draft; writing—review and editing. **Tonino Sophy**: Conceptualization; data curation; formal analysis; funding acquisition; investigation; methodology; project administration; software; supervision; validation; visualization; writing—review and editing. **El Hassane Aglzim**: Data curation; formal analysis; investigation; resources; supervision; validation; writing—review and editing.

ACKNOWLEDGEMENTS

This research is part of the Deliv' Air project funded by the Bourgogne Franche-Comte region, France (Région BFC).

CONFLICT OF INTEREST STATEMENT

The authors declare no conflicts of interest.

DATA AVAILABILITY STATEMENT

Research data are not shared.

ORCID

Charbel Hage https://orcid.org/0000-0003-4729-6825
El Hassane Aglzim https://orcid.org/0000-0002-3998-8787

REFERENCES

1. Mai, Y., Zhao, H., Guo, S.: The analysis of image stabilization technology based on small-UAV airborne video. In: 2012 International Conference on Computer Science and Electronics Engineering, pp. 586–589. IEEE, Piscataway (2012). https://doi.org/10.1109/ICCSEE.2012.77
2. Hoffmann, G., Huang, H., Waslander, S., Tomlin, C.: Quadrotor helicopter flight dynamics and control: Theory and experiment. In: AIAA Guidance, Navigation and Control Conference. AIAA Press, Menlo Park, CA (2007). https://doi.org/10.2514/6.2007-6461
3. Pounds, P., Mahony, R., Corke, P.: Modelling and control of a large quadrotor robot. Control Eng. Pract. 18, 691–699 (2010). https://doi.org/10.1016/j.conengprac.2010.02.008

4. Wild, G., Murray, J., Baxter, G.: Exploring civil drone accidents and incidents to help prevent potential air disasters. Aerospace 3(3), 22 (2016). https://doi.org/10.3390/aerospace3030022
5. Deters, R., Kleinke, S., Selig, M.: Static testing of propulsion elements for small multirotor unmanned aerial vehicles. In: AIAA Applied Aerodynamics Conference. AIAA Press, Menlo Park, CA (2017). https://doi.org/10.2514/6.2017-3743
6. Del Cont Bernard, D., Giurato, M., Riccardi, F., Lovera, M.: Ground effect analysis for a quadrotor platform. In: Dołęga, B., Głębocki, R., Kordos, D., Żugaj, M. (Eds.), Advances in Aerospace Guidance, Navigation and Control, pp. 351–367. Springer International Publishing, Cham (2018)
7. Cheeseman, I.C., Bennett, W.E.: The effect of the ground on a helicopter rotor in forward flight (1955). https://reports.aerade.cranfield.ac.uk/handle/1826.2/3590
8. Bangura, M., Mahony, R.E.: Nonlinear dynamic modeling for high performance control of a quadrotor. In: IEEE International Conference on Robotics and Automation (ICRA 2012). IEEE, Piscataway (2012)
9. Danjun, L., Yan, Z., Zongying, S., Geng, L.: Autonomous landing of quadrotor based on ground effect modelling. In: 2015 34th Chinese Control Conference (CCC), pp. 5647–5652. IEEE, Piscataway (2015). https://doi.org/10.1109/ChiCC.2015.7260521
10. Sanchez-Cuevas, P., Heredia, G., Ollero, A.: Characterization of the aerodynamic ground effect and its influence in multirotor control. Int. J. Aerosp. Eng. 2017, 1–17 (2017). https://doi.org/10.1155/2017/1823056
11. Gao, S., Franco, C.D., Carter, D., Quinn, D., Bezzo, N.: Exploiting ground and ceiling effects on autonomous UAV motion planning. In: 2019 International Conference on Unmanned Aircraft Systems (ICUAS), pp. 768–777. IEEE, Piscataway (2019). https://doi.org/10.1109/ICUAS.2019.8798091
12. He, X., Leang, K.: Quasi-steady in-ground-effect model for single and multirotor aerial vehicles. AIAA J. 58, J059223 (2020). https://doi.org/10.2514/1.J059223
13. McKinnon, C.D., Schoellig, A.P.: Estimating and reacting to forces and torques resulting from common aerodynamic disturbances acting on quadrotors. Rob. Auton. Syst. 123, 103314 (2020). https://doi.org/10.1016/j.robot.2019.103314
14. Ansys, Inc.: Ansys Fluent Theory Guide. Canonsburg, PA (2011)
15. Zhang, T., Wang, Z., Huang, W., Ingham, D., Ma, L., Pourkashanian, M.: A numerical study on choosing the best configuration of the blade for vertical axis wind turbines. J. Wind Eng. Ind. Aerodyn. 201, 104162 (2020). https://doi.org/10.1016/j.jweia.2020.104162.
16. Joo, S., Choi, H., Lee, J.: Aerodynamic characteristics of two-bladed h-darrieus at various solidities and rotating speeds. Energy 90, 439–451 (2015). https://doi.org/10.1016/j.energy.2015.07.051
17. Paz, C., Suárez, E., Gil, C., Vence, J.: Assessment of the methodology for the CFD simulation of the flight of a quadcopter UAV. J. Wind Eng. Ind. Aerodyn. 218, 104776 (2021). https://doi.org/10.1016/j.jweia.2021.104776
18. Kutty, H.A., Rajendran, P.: 3D CFD simulation and experimental validation of small APC slow flyer propeller blade. Aerospace 4(1), 10 (2017). https://doi.org/10.3390/aerospace4010010
19. Stajuda, M., Karczewski, M., Obidowski, D., Jóźwik, K.: Development of a CFD model for propeller simulation. Mech. Mech. Eng. 20, 579–593 (2016)
20. Paz, C., Suárez, E., Gil, C., Baker, C.: Cfd analysis of the aerodynamic effects on the stability of the flight of a quadcopter uav in the proximity of walls and ground. J. Wind Eng. Ind. Aerodyn. 206, 104378 (2020). https://doi.org/10.1016/j.jweia.2020.104378
21. Schiano, F., Alonso-Mora, J., Rudin, K., Beardsley, P., Siegwart, R., Siciliano, B.: Towards estimation and correction of wind effects on a quadrotor UAV. In: IMAV 2014: International Micro Air Vehicle Conference and Competition 2014, pp. 134–141. Sage, New York (2014). https://doi.org/10.3929/ethz-a-010286793
22. Tomić, T., Schmid, K., Lutz, P., Mathers, A., Haddadin, S.: The flying anemometer: Unified estimation of wind velocity from aerodynamic power and wrenches. In: 2016 IEEE/RSJ International Conference on Intelligent Robots and Systems (IROS), pp. 1637–1644. IEEE, Piscataway (2016). https://doi.org/10.1109/IROS.2016.7759264
23. Smeur, E., de Croon, G., Chu, Q.: Cascaded incremental nonlinear dynamic inversion for MAV disturbance rejection. Control Eng. Pract. 73, 79–90 (2018). https://doi.org/10.1016/j.conengprac.2018.01.003
24. Kang, N., Sun, M.: Simulated flowfields in near-ground operation of single and twin-rotor configurations. J. Aircraft 37, 214–220 (2000). https://doi.org/10.2514/2.2609
25. Raza, S.A., Sutherland, M., Etele, J., Fusina, G.: Experimental validation of quadrotor simulation tool for flight within building wakes. Aerosp. Sci. Technol. 67, 169–180 (2017). https://doi.org/10.1016/j.ast.2017.03.043
26. Kaya, K., Özcan, O.: A numerical investigation on aerodynamic characteristics of an air-cushion vehicle. J. Wind Eng. Ind. Aerodyn. 120, 70–80 (2013). https://doi.org/10.1016/j.jweia.2013.06.012
27. Hage, C., Sophy, T., Aglzim, E.H.: Investigating uav propellers performances near moving obstacles: Cfd study, thrust control, and battery energy management. IEEE Open J. Veh. Technol. 4, 590–609 (2023c). https://doi.org/10.1109/OJVT.2023.3309103
28. Hepperle, M.: Propellerscanner. http://mh-aerotools.de. Accessed 2 May 2017
29. Uhlig, D., Selig, M.: Post Stall Propeller Behavior at Low Reynolds Numbers. In: AIAA Aerospace Sciences Meeting and Exhibit. AIAA Press, Menlo Park, CA (2008). https://doi.org/10.2514/6.2008-407
30. Kakimpa, B., Hargreaves, D., Owen, J., Martinez-Vazquez, P., Baker, C., Sterling, M., Quinn, A.: Cfd modelling of free-flight and auto-rotation of plate type debris. Wind Struct. 13(2), 169–189 (2010). https://doi.org/10.12989/was.2010.13.2.169
31. Eckert, M.: The Dawn of Fluid Dynamics: A Discipline Between Science and Technology. Wiley-VCH Verlag GmbH & Co. KGaA, Weinheim (2006). https://doi.org/10.1002/9783527610730
32. Schlatter, P., Örlü, R., Li, Q., Brethouwer, G., Fransson, J., Johansson, A., Alfredsson, P.H., Henningson, D.: Turbulent boundary layers up to Re=2500 studied through simulation and experiment. Phys. Fluids 21, 051702 (2009). https://doi.org/10.1063/1.3139294
33. Jones, W., Launder, B.: The prediction of laminarization with a two-equation model of turbulence. Int. J. Heat Mass Transfer 15, 301–314 (1972). https://doi.org/10.1016/0017-9310(72)90076-2
34. Launder, B., Spalding, D.: The numerical computation of turbulent flows. Comp. Meth. Appl. Mech. Eng. 3, 269–289 (1974). https://doi.org/10.1016/0045-7825(74)90029-2
35. Launder, B., Sharma, B.: Application of energy dissipation model of turbulence to the calculation of flow near spinning disc. Lett. Heat Mass Transfer 1, 131–137 (1974). https://doi.org/10.1016/0735-1933(74)90024-4
36. Rezaeiha, A., Montazeri, H., Blocken, B.: On the accuracy of turbulence models for cfd simulations of vertical axis wind turbines. Energy 180, 838–857 (2019). https://doi.org/10.1016/j.energy.2019.05.053.
37. Hage, C., Sophy, T., Aglzim, E.H.: Cfd analyses of the aerodynamic effects on a quadcopter propeller in the proximity of fixed and horizontal moving obstacles. In: 2023 14th International Conference on Mechanical and Intelligent Manufacturing Technologies (ICMIMT), pp. 273–278. IEEE, Piscataway (2023a). https://doi.org/10.1109/ICMIMT59138.2023.10200614
38. Hage, C., Sophy, T., Aglzim, E.H.: Cfd effect of propellers interference on the thrust variation in the proximity of fixed and horizontal moving obstacle. In: 2023 International Conference on Mechanical, Automotive and Mechatronics Engineering (ICMAME). IEEE, Piscataway (2023b). https://doi.org/10.53375/icmame.2023.191
39. Rabah, M., Haghbayan, H., Immonen, E., Plosila, J.: An ai-in-loop fuzzy-control technique for uav's stabilization and landing. IEEE Access 10, 101109–101123 (2022). https://doi.org/10.1109/ACCESS.2022.3208685

How to cite this article: Hage, C., Sophy, T., Aglzim, E.H.: A comprehensive study on the aerodynamic influence of stationary and moving obstacles on an isolated phantom DJI 3 UAV propeller. J. Eng. 2024, e12374 (2024). https://doi.org/10.1049/tje2.12374